# Online Wind Field Estimation for Airborne Wind Energy Systems in Circular Flight

Jakob Harzer[1,*], Felix Renard[1], Kim Polkläser[2], Dieter Moormann[2], Moritz Diehl[1]
[1]University of Freiburg, Germany, [2]RWTH Aachen University, Germany

## Abstract

Airborne Wind Energy (AWE) systems utilize tethered wings flying high-speed crosswind trajectories to harvest energy from the stronger and more consistent winds available at high altitudes. Knowledge of the local wind field is crucial for maximizing power generation while ensuring flight stability and safety, particularly because these periodic trajectories remain spatially confined. In this work, we estimate the parameters of a wind field model capturing both shear and veer during the online operation of an AWE system flying periodic circular orbits, utilizing an Extended Kalman Filter (EKF). We then use these estimates in a Nonlinear Model Predictive Control (NMPC) scheme based on a dynamic model that incorporates the spatially varying wind field. We demonstrate in a simulation study that the proposed approach accurately estimates sudden variations in the wind parameters during online closed-loop tracking while satisfying operational flight envelope constraints.

## 1 Introduction

Airborne wind energy (AWE) systems produce renewable electric energy by harvesting wind using tethered wings at high altitudes where, compared to traditional wind turbines, the available wind is stronger and more consistent. The systems fly acrobatic crosswind maneuvers at high speeds and thus generate large aerodynamic forces which are converted to usable electric energy using one of two approaches: Systems operating in 'drag-mode' transfer the electricity from onboard propeller generators to the ground via the tether, whereas in systems operating in 'pumping-mode', the tether drum is connected to a generator on the ground. Here, the tether is reeled out at high tether force to produce energy and reeled back in with low tether force in a periodic pumping motion. The technology promises renewable energy generation with less material investment and ground use compared to traditional wind energy [1]. In Figure 1, we show both an example of a 'soft-wing' system in pumping mode as well as a 'rigid-wing' system in drag mode. For more information on airborne wind energy we refer the reader to [4].

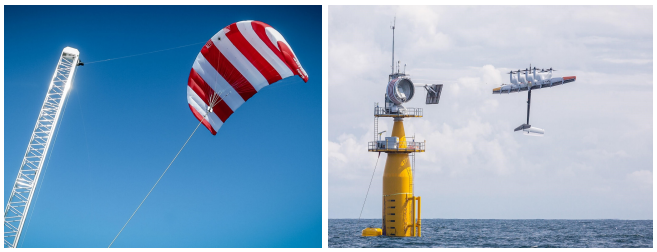

Figure 1: Left: Skysails PN-14 soft-wing system from [2], right: Makani M600 drag-mode rigid-wing system, from [3].

The tethered flight systems typically operate on flight trajectories in a limited spatial range, which are optimized based on a chosen model of the local wind field. While for planning purposes complex wind fields are considered [5], for the online closed-loop operation simpler wind field models are commonly used. We propose to estimate the fluctuating parameters of a complex model of the current wind field with altitude-dependent wind speed and direction online using an Extended Kalman Filter (EKF). To make use of the estimates, a controller with knowledge about the spatially changing wind field is required, for which we propose to use a Nonlinear Model Predictive Controller (NMPC). Equipped with an accurate wind field model, such a predictive controller is expected to have better tracking performance compared to a controller that does not know about the spatially changing wind conditions. We visualize the idea in Figure 2, where we show both the wind field used to generate the tracking reference as well as the actual wind-field whose wind direction and magnitude are altitude-dependent. The forward prediction horizon of the NMPC is visualized originating from the tethered flight system's current position.

State and wind estimation for airborne wind energy systems has been subject to prior research. Typically, the available measurements contain positions and velocities from GPS measurements, orientations, their rates, and accelerations from an IMU, airspeed from Pitot tubes as well as the tether force and angle. With well-established methods such as EKF, unscented Kalman filters or moving-horizon estimation, these measurements can be fused into state and wind estimates [6–8]. We refer the reader to Table 1 in [6] for an overview. The wind field estimate typically consists of

*Corresponding author email: jakob.harzer@imtek.uni-freiburg.de. This research was supported by DFG via projects 504452366 (SPP 2364), 560056112 (robust MPC), 535860958 (ALeSCo), 525018088 (MAWERO) and 545539514, and by BMWK via 03EN3054B.

http://www.imavs.org/

http://www.imavs.org/

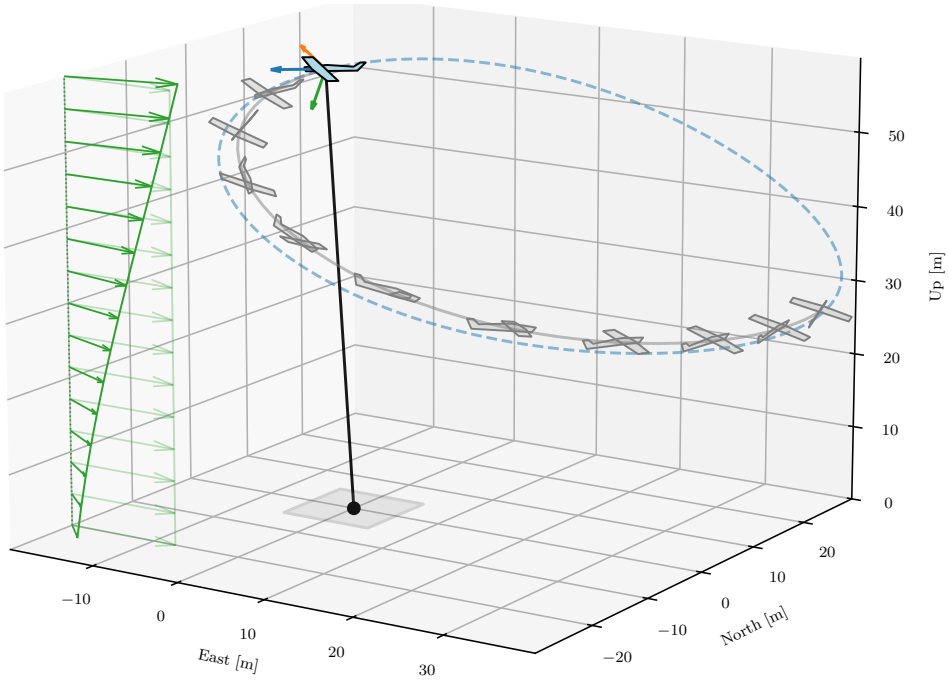


Figure 2: The closed-loop NMPC controller uses an EKF estimate of the actual wind field that might differ from the one used for the reference trajectory generation

wind direction and magnitude [9, 10] or parameters of a one-dimensional logarithmic wind-shear model with known direction [11]. In [6], the wind speed and direction variability in space and time is handled by assuming appropriate process noise on the parameter estimates. Such estimates of the wind field parameters can be used to adjust the periodic flight orbit to changing conditions [11, 12], but require a dynamic model of the system [10]. Particularly suited for the inclusion of complex wind models are NMPC control schemes which offer out-of-the-box satisfaction of system constraints, but only have been used in combination with simple wind models [7, 8]. This work attempts to bridge this gap by estimating the parameters of a wind field with both shear and veer and utilizing the estimation in a predictive controller.

We introduce an AWE system model in Section 2 and describe the closed-loop control and wind-state estimation in Section 3. We showcase the performance of the approach in Section 4 and conclude the paper with Section 5.

## 2 System Model

In the following, we develop a model to describe the tethered rigid-wing AWE system with RWTH Aachen's "Maverix" flight system. The Maverix is a versatile, multi-purpose flight-system with a wingspan of $1.5\,\mathrm{m}$ and a mass of $2.4\,\mathrm{kg}$. Figure 3 shows a render of the flight system. In this paper, we consider it to be connected to the origin with a tether of constant length $l = 50\,\mathrm{m}$. The flight system has propellers on both its wings. Although in an AWE setup we do not want to spend additional energy for propulsion, we still include the propeller thrust in the dynamic model and also utilize them in the reference solution and for feedback control. The Maverix flight system also has vertical liftoff and landing capabilities, which are disregarded in the model.

### 2.1 State-Space Model

The following is largely based on [5, 13]. We model the AWE system with the state vector

$$x = [r, \dot{r}, R, \omega, \xi, \eta, \sigma_r, \sigma_l]^\top \in \mathbb{R}^{22} \tag{1}$$

where $r = [r_x, r_y, r_z]^\top \in \mathbb{R}^3$ is the position of the flight system in a north-east-down (NED) inertial frame $(e_x, e_y, e_z)$, $\dot{r} \in \mathbb{R}^3$ is its velocity in the same NED inertial frame, $R \in \mathrm{SO}(3) \subset \mathbb{R}^9$ is a direction-cosine rotation matrix describing the attitude and $\omega \in \mathbb{R}^3$ is the vector of angular velocities in the NED body frame. The state vector is extended with actuator states for the ailerons on the left and right wings, which are assumed to be actuated symmetrically with angle $\xi = \xi_l = -\xi_r$, an elevator flap angle $\eta$ and left and right propellors' forward thrusts $\sigma_r, \sigma_l$. The considered control vector is then simply given as the rates of the actuator states:

$$u = [\dot{\xi}, \dot{\eta}, \dot{\sigma}_r, \dot{\sigma}_l] \in \mathbb{R}^4 \tag{2}$$

Following [5, 7, 13], we derive the dynamic model of the tethered AWE system using Lagrangian dynamics. For this,

http://www.imavs.org/

Figure 3: Render of RWTH Aachen's Maverix flight system

we introduce an algebraic variable $z \in \mathbb{R}$ that is proportional to the tether pulling force with magnitude $|F_\mathrm{t}| = zl$. The system dynamics in fully implicit form are then:

$$0 = f(\dot{x}, x, z, u, p) \tag{3}$$

where the vector $p \in \mathbb{R}^{n_p}$ contains the parameters of the model, in this case explicitly the coefficients of the wind field discussed below. In contrast to [5, 7, 13], for simplicity we omit tether drag forces, and the tether is assumed to be of constant length. The model has the algebraic tether constraint $c(x) = r^\top r - l^2 = 0$ which implies a "rigid" tether and requires $z > 0$ for validity. Since with this algebraic state constraint, the dynamics would be an index-3 differential-algebraic equation (DAE), we apply index reduction to modify the dynamics into an index-1 DAE whose solution satisfies the tether and rotation matrix invariants:

$$c(x) = 0, \quad \dot{c}(x) = 0, \quad c_R(x) = P_\mathrm{u}\big(R^\top R - \mathbb{I}_3\big) = 0, \tag{4}$$

where the operator $P_\mathrm{u}$ selects the upper triangular elements of the matrix. Thus, at the initial state of a numerical simulation, these consistency conditions have to be satisfied explicitly. To avoid drifting of the invariants due to numerical instability, we use a Baumgarte stabilization scheme. We refer the reader to [5, 13] for further details on the exact model dynamics.

### 2.2 *Wind Model*

We assume a wind field where the wind: (a) only changes with altitude, and (b) does not have a vertical component (i.e., the wind is always horizontal). In particular, we consider the following model that captures both wind shear and wind veer:

$$v_w(r_z, p) = \begin{bmatrix} \cos(p_1 + p_4(r_z - z_0)) \\ \sin(p_1 + p_4(r_z - z_0)) \\ 0 \end{bmatrix} (p_2 + p_3(r_z - z_0)) \tag{5}$$

where the four scalar parameters $p = [p_1, p_2, p_3, p_4]^\top$ take the meaning of the wind direction $p_1$ and speed $p_2$ at a reference height $z_0$ and the gradients $p_4$, $p_3$ of the direction and the speed with respect to the altitude $r_z$, respectively.

### 2.3 *Aerodynamics*

To compute the aerodynamic forces and moments for the particular flight system considered in this paper we use an element-based simulation model which divides the aircraft into individual aerodynamic surfaces. The simulation computes the force and moment vectors for each element for a given local airspeed, angular velocity and actuator deflection and calculates the total forces and moments affecting the system in the body-fixed coordinate frame. This element-based method includes aerodynamic effects such as induced drag, lift, and propeller slipstream and is suited for a tilt-wing aircraft, as is considered in this paper. An detailed description of the element-based modeling method can be found in [14].

For the flight path trajectory optimization, in particular for the online predictive control scheme, we require a differentiable low-fidelity model. For the given flight system, we obtain this low-fidelity model by sampling the 11-dimensional input space of the simulation model over a large range of flight states to capture the complex nonlinear model dynamics within a simplified data set. This data set contains approximately 13 million data points, each representing a different operating point. Subsequently, we fit a low-order polynomial onto the data where we choose the 71 polynomial regressors such that they include known aerodynamic quantities, for example the squared airspeed or the angle of attack. Since the model should require as few computations as possible, we solve a sparse linear least-squares fitting problem for each individual component of the forces and moments vectors using an extended Gauss-Newton method [15]. The polynomial approximations with up to 35/71 non-zero coefficients show a good fit on the 20% test split of the data with a standard deviation of the residuals less than 4 % for each component.

### 2.4 *System Constraints*

We have tight constraints on the flight envelope of the Maverix flight system, and thus require the satisfaction of nonlinear and linear state and control constraints given in Table 1. Here,

$$v_\mathrm{b} = R^\top(\dot{r} - v_w(r_z, p)) \tag{6}$$

is the velocity vector in the body-fixed coordinate system relative to the airflow, $\alpha = \mathrm{atan2}(v_{\mathrm{b},z}, v_{\mathrm{b},x})$ is the angle of attack, $\beta = \mathrm{atan2}(v_{\mathrm{b},y}, v_{\mathrm{b},x})$ is the sideslip angle and $\gamma = \cos^{-1}(-l^{-1} r^\top R e_z)$ is the angle between the tether vector and the flight systems upward orientation unit vector, which we constrain to avoid the collision of the flight system with the tether. We collect all nonlinear and linear state and control constraints as

$$h_\mathrm{min} \leq h(x, z, p) \leq h_\mathrm{max} \tag{7a}$$
$$x_\mathrm{min} \leq x \leq x_\mathrm{max} \tag{7b}$$
$$u_\mathrm{min} \leq u \leq u_\mathrm{max} \tag{7c}$$

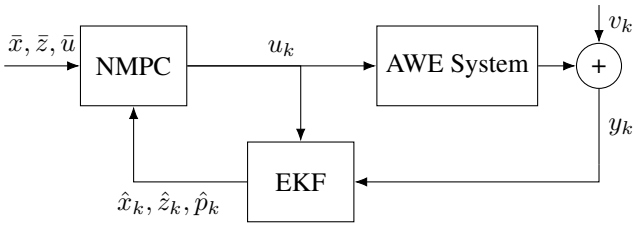


Figure 4: Closed-loop simulation

### 2.5 *Measurements*

We assume that the flight system is equipped with sensors that provide the measurements

$$g(x, z, p) = \begin{bmatrix} r \\ \dot{r} \\ \omega \\ \|v_\mathrm{b}\|_2 \\ R^\top(\ddot{r} - a_g) \\ F_t \end{bmatrix} \tag{8}$$

including an GPS measurement of position and velocity, an IMU measurement of angular velocity in the body frame, an airspeed measurement, an IMU measurement of acceleration in the body frame, as well as a measurements of the tether force. Here, $a_g = [0, 0, 9.81]^\top \mathrm{m/s^2}$ is the gravitational acceleration in the NED inertial frame. The measurements are summarized in Table 2 where we follow [7] for their standard deviation values, except for the force measurement where we assume a standard deviation of $1\,\mathrm{N}$.

## 3 CLOSED-LOOP WIND PARAMETER ESTIMATION

In order to estimate the wind parameters $p$ in online operation of the tethered flight system, we consider the following closed-loop approach visualized in Figure 4. The available noisy measurements from the system, as well as the applied control $u_k$, are used by an Extended Kalman Filter (EKF) to obtain both a state estimate $\hat{x}_k, \hat{z}_k$ and an estimate for the wind parameters $\hat{p}_k$. A Nonlinear Model Predictive Controller (NMPC) generates a feedback control signal such that the tethered system follows a pre-computed reference state and control trajectories $\bar{x}, \bar{z}, \bar{u}$. We assume that we obtain a measurements every $\delta_1 = 10\,\mathrm{ms}$, for which we obtain a new state estimate from the EKF. The NMPC is sampled every $\delta_2 = 10\delta_1 = 100\,\mathrm{ms}$ and predicts $N = 50$ intervals into the future, which corresponds to a horizon of $N\delta_2 = 5\,\mathrm{s}$.

### 3.1 *Model Discretization*

We discretize the continuous model as follows: For a discrete time point $t_k$ on a time-grid with step size $\delta$, consider the approximations $x_k \approx x(t_k), z_k \approx z(t_k)$. We assume that over a discretization interval $t \in [t_k, t_k + \delta]$, the control $u(t) = u_k$ is held constant. The fully implicit index-1 differential-algebraic equation system (3) is integrated using an implicit Runge-Kutta scheme with a collocation Gauss-Radau IIA method which is well-suited for the stiff dynamics. Since the last of the three collocation nodes is at the end of the interval, the algebraic state $z_{k+1}$ is uniquely determined from the state values and does not depend on $z_k$. We then have the discrete deterministic model:

$$0 = F_\delta(x_{k+1}, z_{k+1}, x_k, u_k, p), \tag{9}$$

and, by incorporating measurements, the discrete stochastic model:

$$0 = F_\delta(x_{k+1}, z_{k+1}, x_k, u_k, p) \tag{10a}$$
$$y_k = g(x_k, z_k, p) + v_k \tag{10b}$$

Here, the measurement noise is $v_k \sim \mathcal{N}(0, V)$ for whose covariance matrix $V$ is built from the standard deviations given in Table 2. Note that we do not consider any state noise.

### 3.2 *Reference Trajectory Generation*

For the tracking reference, we generate dynamically feasible periodic state and control trajectories for the system by formulating and solving an optimal control problem with direct collocation where we use the simple constant wind-model with $p_1 = 90°, p_2 = 5\,\mathrm{m/s}, p_3 = 0/\mathrm{s}, p_4 = 0\,°/\mathrm{m}$. We obtain the $T$-periodic references:

$$\bar{x} : \mathbb{R} \to \mathbb{R}^{n_x}, \qquad \bar{x}(t + T) = \bar{x}(t), \tag{11a}$$
$$\bar{z} : \mathbb{R} \to \mathbb{R}^{n_z}, \qquad \bar{z}(t + T) = \bar{z}(t), \tag{11b}$$
$$\bar{u} : \mathbb{R} \to \mathbb{R}^{n_u}, \qquad \bar{u}(t + T) = \bar{u}(t). \tag{11c}$$

Typically, we want the AWE system to follow power-optimal flight trajectories [5], but the considered experimental proof-of-concept system based on the Maverix flight system is not intended to generate energy. Thus, we consider the objective of a large, constant tether force as proxy for the objective of producing power. We then design the optimal control problems cost accordingly such that we obtain a smooth circular trajectory with radius $\approx 50\,\mathrm{m}$ that is tilted 30° to the east, with almost constant tether force of $\approx 50\,\mathrm{N}$ and a period duration of $T \approx 11\,\mathrm{s}$. We use slightly tightened aerodynamic bounds to account for disturbances in the later online tracking.

### 3.3 *Model Predictive Control Scheme*

To exploit the wind field estimates in closed-loop operation, we employ an NMPC scheme equipped with the discretized dynamical model (9). At any time $t_0$, we have the NMPC horizon as the uniform time grid: $t_k = t_0 + k\delta_2, k = 1, \ldots, N$ with $N = 50$ intervals. Note that this grid is different from the simulation time grid above. The controller tries to track the pre-calculated reference trajectories by sampling them as:

$$\bar{x}_k = \bar{x}(t_k), \qquad \bar{z}_k = \bar{z}(t_k), \qquad \bar{u}_k = \bar{u}(t_k), \tag{12}$$

http://www.imavs.org/

http://www.imavs.org/

where the tracking cost terms are weighted by

$$Q = \mathrm{diag}(Q_x, Q_z, Q_u), \tag{13a}$$
$$Q_\mathrm{f} = \mathrm{diag}(Q_x, Q_z), \tag{13b}$$

where the values of the diagonal matrices, given in Table 4, are chosen to emphasize the tracking of the tether force vector with small deviations in angular rates and flap controls. For a given state and parameter estimate $(\hat{x}, \hat{z}, \hat{p})$ at some time $t_0$, we then solve the NMPC problem:

$$\min_{\substack{x_0,\dots,x_N\\ z_0,\dots,z_N\\ u_0,\dots,u_{N-1}}} \sum_{k=0}^{N-1} \left\| \begin{matrix} x_k - \bar{x}_k \\ z_k - \bar{z}_k \\ u_k - \bar{u}_k \end{matrix} \right\|_Q^2 + \left\| \begin{matrix} x_N - \bar{x}_N \\ z_N - \bar{z}_N \end{matrix} \right\|_{Q_\mathrm{f}}^2 \tag{14a}$$
$$\text{s.t.} \quad x_0 = \hat{x}, \tag{14b}$$
$$z_0 = \hat{z}, \tag{14c}$$
$$0 = F_{\delta_2}(x_{k+1}, x_k, z_{k+1}, u_k, \hat{p}), \quad \forall k \in \mathcal{K}_{N\text{-}1}, \tag{14d, 14e}$$
$$u_\mathrm{min} \le u_k \le u_\mathrm{max}, \quad \forall k \in \mathcal{K}_{N\text{-}1}, \tag{14f}$$
$$x_\mathrm{min} \le x_k \le x_\mathrm{max}, \quad \forall k \in \mathcal{K}_N, \tag{14g}$$
$$h_\mathrm{min} \le h(x_k, z_k, \hat{p}) \le h_\mathrm{max}, \forall k \in \mathcal{K}_N \tag{14h}$$

where $\mathcal{K}_N = \{0, 1, \dots, N\}$ and $\mathcal{K}_{N-1}$ are index sets and we re-introduce the discrete states $x_k, z_k, u_k$ for the NMPC problem. The control and state constraints are enforced as hard constraints, while the nonlinear constraints are implemented as soft constraints with slack variables and an associated penalty to improve problem feasibility. We solve problem (14) with the fast embedded NMPC solver acados [16] in combination with the CasADi [17] framework, where we use the advanced-step real-time iteration scheme [18] with a single sequential quadratic programming (SQP) step per sampling instant. The solver is configured with a Gauss–Newton Hessian approximation and a partial-condensing quadratic-program solver "HPIPM" [19]. The first computed control $u_0$ is then returned to the plant as the closed-loop feedback.

### *3.4 State and Wind Parameter Estimation*

The dynamics of the system (3) contain algebraic conditions as well as consistency conditions that need to be satisfied by the state estimates, for which a conventional EKF implementation is not suitable. Instead, we follow [20] for details on EKF estimation with index-1 DAE systems. For the estimation of both the state and the wind field parameters, it is convenient to augment the state vector and dynamics with a parameter state $\dot{p} = 0$ as $x^a = [x, p]^\top \in \mathbb{R}^{n_x+n_p}$. Additionally, we can explicitly split the fully implicit index-reduced DAE into differential and algebraic parts. We then obtain the model in semi-explicit form:

$$\dot{x}^a = f^a_\mathrm{ode}(x^a, z, u), \tag{15a}$$
$$0 = f_\mathrm{alg}(x^a, z, u). \tag{15b}$$

The state update based on the linearization of the function $g$ might violate the consistency conditions. To counteract this, we also augment the measurements with a pseudo-measurement of the consistency conditions following [21], similar to [22]:

$$y^a = g^a(x, z) = \begin{bmatrix} g(x, z, p) \\ c(x) \\ \dot{c}(x) \\ c_R(x) \end{bmatrix} \tag{16}$$

For the EKF prediction step, we propagate the current (augmented) estimates $\hat{x}^a_{k|k}, \hat{z}_{k|k}$ of the differential and algebraic states using the implicit Runge-Kutta integration method on the dynamics (15) similar to Equation (9) to obtain predicted $\hat{x}^a_{k+1|k}, \hat{z}_{k+1|k}$. In order to propagate the uncertainty covariances of both the augmented differential state and algebraic state $P_k \in \mathbb{R}^{(n_x+n_p+n_z)\times(n_x+n_p+n_z)}$, we linearize the semi-explicit DAE at the current estimate:

$$A = \begin{bmatrix} \frac{\partial f_\mathrm{ode}}{\partial x^a} & \frac{\partial f_\mathrm{ode}}{\partial z} \\ \frac{\partial f_\mathrm{alg}}{\partial x^a} & \frac{\partial f_\mathrm{alg}}{\partial z} \end{bmatrix}_{\hat{x}^a_{k|k}, \hat{z}_{k|k}, u_k} \tag{17}$$

and with $\phi = \exp(\Delta t A)$ we propagate the covariance matrices as:

$$P_{k+1|k} = \phi P_{k|k} \phi^\top + \Gamma W \Gamma^\top \tag{18}$$

where

$$\Gamma = \begin{bmatrix} \mathbb{I}_{n_x+n_p} \\ -\left(\frac{f_\mathrm{alg}}{\partial z}\right)^{-1} \frac{\partial f_\mathrm{alg}}{\partial x^a} \end{bmatrix}_{\hat{x}^a_{k|k}, \hat{z}_{k|k}, u_k} \tag{19}$$

and where $W$ is the covariance matrix of the augmented state noise with values from Table 3. For the EKF update step, we correct the differential state estimate

$$\begin{bmatrix} \hat{x}^a_{k+1|k+1} \\ \hat{z}_{k+1|k+1} \end{bmatrix} = \begin{bmatrix} \hat{x}^a_{k+1|k} \\ \hat{z}_{k+1|k} \end{bmatrix} \tag{20}$$
$$+ K_{k+1} \left( y^a_{k+1} - g^a(\hat{x}^a_{k+1|k}, \hat{z}_{k+1|k}) \right) \tag{21}$$

with the measurement augmented with the zero pseudo-measurement for the consistency conditions as $y^a_{k+1} = [y_{k+1}, 0, \dots, 0]^\top$. The covariance matrix is updated as

$$P_{k+1|k+1} = (\mathbb{I} - K_{k+1} G_{k+1}) P_{k+1|k} \tag{22}$$

based on the Kalman gain

$$K_{k+1} = \left( P^{-1}_{k+1|k} + G^\top_{k+1} V_k^{-1} G^\top_{k+1} \right)^{-1} G^\top_{k+1} V_k^{-1} \tag{23}$$

with the linearization of the measurement function $G_{k+1} = \frac{\partial g^a}{\partial (x^a, z)}(\hat{x}^a_{k+1|k}, \hat{z}_{k+1|k})$.

http://www.imavs.org/

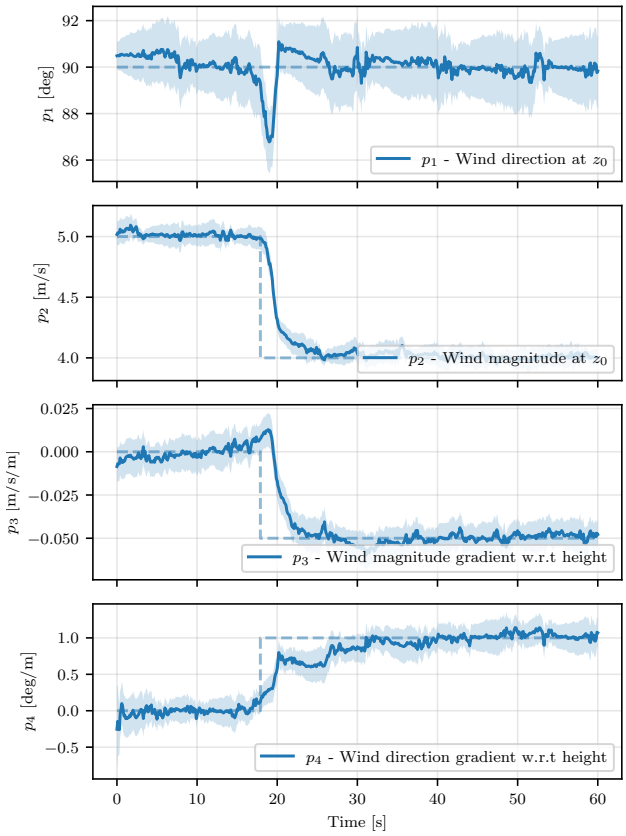


Figure 5: Convergence of the wind parameter estimates during the closed-loop simulation

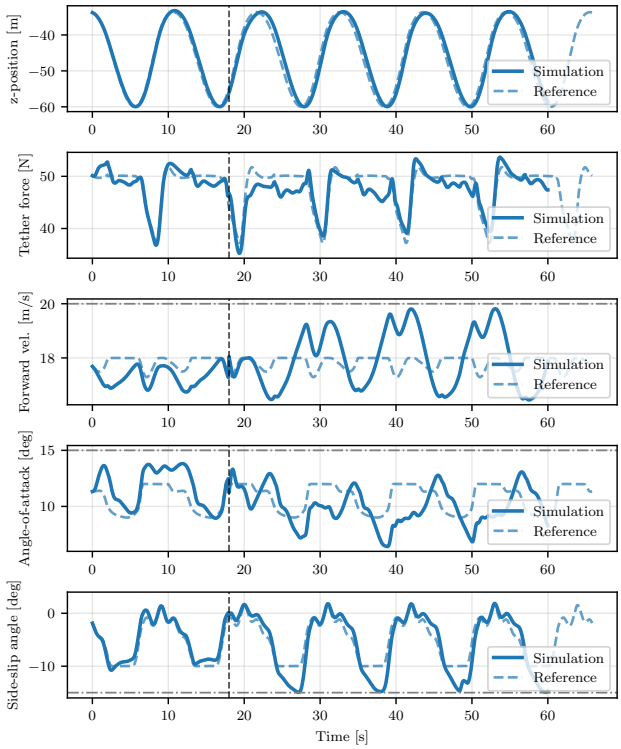


Figure 6: Comparison between implemented simulation and the tracking reference

## 4 SIMULATION EXPERIMENTS

To demonstrate the approach, we perform a simulation of the closed-loop system where the tethered flight system should follow the generated circular tilted reference. In the scenario, the wind conditions are the same as in the reference generation at first, but after 18 s, the conditions jump to a more complex wind field:

$$p(t) = \begin{cases} [90°, 5\,\mathrm{m/s}, 0/\mathrm{s}, 0\,°/\mathrm{m}]^\top & \text{for } t < 18\,\mathrm{s} \\ [100°, 4\,\mathrm{m/s}, -0.06/\mathrm{s}, 1\,°/\mathrm{m}]^\top & \text{for } t \geq 18\,\mathrm{s} \end{cases} \tag{24}$$

where the wind speed drops by 1 m/s] and there is now both a gradient in the speed and in the direction. We draw an initial state estimate from distribution: $\hat{x}_0^a \sim \mathcal{N}(x_0^a, P_0)$ where the EKF's initial covariance matrix $P_0$ is given from the value in Table 3, and the simulation's initial value is given by $x_0^a = [\bar{x}(0), p(0)]^\top$.

Figure 5 shows the wind field parameter estimates, which closely follow the true values. Figure 6 compares the simulation with the tracked reference trajectory. The state that are supposed to be tracked by the NMPC (e.g.$z$-position and tether force) closely follow the reference. In the first few seconds after the wind field changes, the wind-field estimate is not converged yet. Since the tether force is very sensitive to the wind conditions, the NMPC struggles to maintain the tracked tether forces (second plot in Figure 6) at first but later compensates for the wind conditions by increasing the peak forward velocity (third plot). After the wind field estimates have converged to the new conditions, the nonlinear aerodynamic envelope constraints remain satisfied (bottom three plots in Figure 6), even though perfect tracking of the reference is no longer achieved.

## 5 CONCLUSION

In this paper, we outlined a closed-loop estimation approach of the parameters of a shear and veer wind field model for an airborne wind energy system operating in periodic circular orbits. In a simulation of a proof-of-concept setup with the 'Maverix' flight system, we can accurately estimate the wind field parameters. The NMPC scheme utilizes these estimates to satisfy nonlinear flight envelope constraints while still tracking the reference trajectory.

**Acknowledgments** We thank Johannes Schuler, Bagasprawira Herlambang, Katrin Baumgärtner, and Jonathan Frey for their support during the writing process. For this publication, large language models were used for code generation, literature research, and grammar checks.

http://www.imavs.org/

The authors claim full responsibility for the contents of the publication.

## REFERENCES

[1] Jochem De Schutter, Jakob Harzer, and Moritz Diehl. Vertical Airborne Wind Energy Farms with High Power Density per Ground Area based on Multi-Aircraft Systems. *European Journal of Control*, 74:100867, November 2023.

[2] SkySails Power GmbH. Skysails power gmbh website. https://skysails-power.com/, 2024. Accessed: 2024-11-13.

[3] Roland Schmehl and Oliver Tulloch, editors. *8th International Airborne Wind Energy Conference (AWEC 2019): Book of Abstracts*. Delft University of Technology / University of Strathclyde, 2019.

[4] Uwe Ahrens, Moritz Diehl, and Roland Schmehl, editors. *Airborne Wind Energy*. Green Energy and Technology. Springer Berlin, Heidelberg, 2013.

[5] J. De Schutter, R. Leuthold, T. Bronnenmeyer, E. Malz, S Gros, and M. Diehl. AWEbox: An optimal control framework for single- and multi-aircraft airborne wind energy systems. *Energies*, 16(4):1900, 2023.

[6] Oriol Cayon, Simon Watson, and Roland Schmehl. Kite as a Sensor: Wind and State Estimation in Tethered Flying Systems, January 2025.

[7] Mario Zanon, Greg Horn, Sebastien Gros, and Moritz Diehl. Control of Dual-Airfoil Airborne Wind Energy systems based on nonlinear MPC and MHE. In *2014 European Control Conference (ECC)*, pages 1801–1806, Strasbourg, France, June 2014. IEEE.

[8] Sébastien Gros, Mario Zanon, Milan Vukov, and Moritz Diehl. Nonlinear MPC and MHE for Mechanical Multi-Body Systems with Application to Fast Tethered Airplanes. *IFAC Proceedings Volumes*, 45(17):86–93, 2012.

[9] Paul Williams, Bas Lansdorp, and Wubbo Ockels. Nonlinear Control and Estimation of a Tethered Kite in Changing Wind Conditions. *Journal of Guidance, Control, and Dynamics*, 31(3):793–799, May 2008.

[10] Maximilian Ranneberg. Sensor Setups for State and Wind Estimation for Airborne Wind Energy Converters, September 2013.

[11] Aldo U. Zgraggen, Lorenzo Fagiano, and Manfred Morari. Real-Time Optimization and Adaptation of the Crosswind Flight of Tethered Wings for Airborne Wind Energy. *IEEE Transactions on Control Systems Technology*, 23(2):434–448, March 2015.

[12] Mitchell K. Cobb, Kira Barton, Hosam Fathy, and Chris Vermillion. Iterative Learning-Based Path Optimization for Repetitive Path Planning, With Application to 3-D Crosswind Flight of Airborne Wind Energy Systems. *IEEE Transactions on Control Systems Technology*, 28(4):1447–1459, July 2020.

[13] Sébastien Gros and Moritz Diehl. Modeling of Airborne Wind Energy Systems in Natural Coordinates. In Uwe Ahrens, Moritz Diehl, and Roland Schmehl, editors, *Airborne Wind Energy*, pages 181–203. Springer Berlin Heidelberg, Berlin, Heidelberg, 2013.

[14] Philipp Hartmann. Vorausschauende Flugbahnregelung für Kippflügelflugzeuge. Deutscher Luft- und Raumfahrt Kongress 2018, Friedrichshafen (Germany), 4 Sep 2018 - 6 Sep 2018, September 2018.

[15] Katrin Baumgartner and Moritz Diehl. The Extended Gauss-Newton Method for Nonconvex Loss Functions and its Application to Time-Optimal Model Predictive Control. In *2022 American Control Conference (ACC)*, pages 4973–4978, Atlanta, GA, USA, June 2022. IEEE.

[16] Robin Verschueren, Gianluca Frison, Dimitris Kouzoupis, Jonathan Frey, Niels van Duijkeren, Andrea Zanelli, Branimir Novoselnik, Thivaharan Albin, Rien Quirynen, and Moritz Diehl. acados – a modular open-source framework for fast embedded optimal control. *Mathematical Programming Computation*, pages 147–183, 2021.

[17] Joel A E Andersson, Joris Gillis, Greg Horn, James B Rawlings, and Moritz Diehl. CasADi – A software framework for nonlinear optimization and optimal control. 11(1):1–36, 2019.

[18] Jonathan Frey, Armin Nurkanović, and Moritz Diehl. Advanced-Step Real-Time Iterations With Four Levels – New Error Bounds and Fast Implementation in acados. *IEEE Control Systems Letters*, 8:1703–1708, 2024.

[19] Gianluca Frison and Moritz Diehl. HPIPM: A high-performance quadratic programming framework for model predictive control. *IFAC-PapersOnLine*, 53(2):6563–6569, 2020.

[20] Parham Mobed, Sudhakar Munusamy, Debangsu Bhattacharyya, and Raghunathan Rengaswamy. State and Parameter Estimation in Distributed Constrained Systems. 1. Extended Kalman Filtering of a Special Class of Differential-Algebraic Equation Systems. *Industrial & Engineering Chemistry Research*, 56(1):206–215, January 2017.

[21] D. Simon. Kalman filtering with state constraints: A survey of linear and nonlinear algorithms. *IET Control Theory & Applications*, 4(8):1303–1318, August 2010.

[22] Eduardo Schmidt, Marcelo De Lellis Costa De Oliveira, Ramiro Saraiva Da Silva, Lorenzo Fagiano, and Alexandre Trofino Neto. In-Flight Estimation of the Aerodynamics of Tethered Wings for Airborne Wind Energy. *IEEE Transactions on Control Systems Technology*, 28(4):1309–1322, July 2020.

## A TABLES

Table 1: Nonlinear and linear state and control constraints

| Constraint - Nonlinear | Min | Quantity | Max |
|---|---|---|---|
| Longitudinal vel. | $12\,\mathrm{m/s}$ | $v_{\mathrm{b},x}$ | $20\,\mathrm{m/s}$ |
| Lateral / vertical vel. | $-7\,\mathrm{m/s}$ | $v_{\mathrm{b},y}, v_{\mathrm{b},z}$ | $7\,\mathrm{m/s}$ |
| Angle of attack | $-8°$ | $\alpha$ | $15°$ |
| Sideslip angle | $-15°$ | $\beta$ | $15°$ |
| Tether force | $0\,\mathrm{N}$ | $\lvert F_{\mathrm{t}}\rvert$ | $-$ |
| Tether collision | - | $\gamma$ | $90°$ |
| **Constraint - Linear** | **Min** | **Quantity** | **Max** |
| Angular velocities | $-1\,\mathrm{rad/s}$ | $\omega_x, \omega_y, \omega_z$ | $1\,\mathrm{rad/s}$ |
| Aileron angle $\xi$ | $-25°$ | $\xi$ | $25°$ |
| Elevator angle $\eta$ | $-32°$ | $\eta$ | $32°$ |
| Thrust forces | $0\,\mathrm{N}$ | $\sigma_r, \sigma_l$ | $20\,\mathrm{N}$ |
| Elev./Ail. rates | $-25\,°/\mathrm{s}$ | $\dot{\xi}, \dot{\eta}$ | $25\,°/\mathrm{s}$ |
| Thrust force rates | $-5\,\mathrm{N/s}$ | $\dot{\sigma}_r, \dot{\sigma}_l$ | $5\,\mathrm{N/s}$ |

Table 2: Available Measurements, comp. [7]

| Measurement | Quantity | $\sigma$ | Unit |
|---|---|---|---|
| GPS position | $r$ | 0.1 | m |
| GPS velocities | $\dot{r}$ | 0.6 | m/s |
| Angular velocities | $\omega$ | 0.02 | rad/s |
| Airspeed | $\lVert v_{\mathrm{b}}\rVert_2$ | 1 | m/s |
| Accelerations | $R^\top(\ddot{r} - a_g)$ | 0.05 | $\mathrm{m/s^2}$ |
| Tether Force | $\lvert F_{\mathrm{t}}\rvert$ | 1 | N |

Table 3: EKF State Noise Weight and Initial Covariance Values

| State | Process Noise $\sigma$ | Init. Cov. $\sigma$ | Unit |
|---|---|---|---|
| $r$ | 0.01 | 1 | m |
| $\dot{r}$ | 0.1 | 0.5 | m/s |
| $R$ | 0.01 | 0.1 | - |
| $\omega$ | 0.1 | 0.05 | rad/s |
| $\xi, \eta$ | 0.1 | 0.1 | rad |
| $\sigma_{\mathrm{r}}, \sigma_{\mathrm{l}}$ | 0.1 | 0.05 | N |
| $p_1$ | 0.01 | 0.01 | m |
| $p_2$ | 0.05 | 0.1 | m/s |
| $p_3$ | 0.005 | 0.01 | m/(s m) |
| $p_4$ | 0.002 | 0.01 | rad/s |

Table 4: NMPC State and Control Weights

| State/Control | Value | Unit |
|---|---|---|
| $r$ | 0.001 | $1/\mathrm{m}^2$ |
| $\dot{r}$ | 0.1 | $\mathrm{s}^2/\mathrm{m}^2$ |
| $R$ | 1 | - |
| $\omega$ | 50 | $\mathrm{s}^2/\mathrm{rad}^2$ |
| $\xi, \eta$ | 0.001 | $1/\mathrm{rad}^2$ |
| $\sigma_{\mathrm{r}}, \sigma_{\mathrm{l}}$ | 0.001 | $1/\mathrm{N}^2$ |
| $z$ | 50 | $\mathrm{m}^2/\mathrm{N}^2$ |
| $\dot{\xi}$ | 1 | $\mathrm{s}^2/\mathrm{rad}^2$ |
| $\dot{\eta}$ | 1 | $\mathrm{s}^2/\mathrm{rad}^2$ |
| $\dot{\sigma}_{\mathrm{r}}$ | 100 | $\mathrm{s}^2/\mathrm{N}^2$ |
| $\dot{\sigma}_{\mathrm{l}}$ | 100 | $\mathrm{s}^2/\mathrm{N}^2$ |

http://www.imavs.org/